Automated Photographic Grading of Vitreous Haze in Uveitis

by

Serhat Varolgüneş

A Thesis Submitted to the
Graduate School of Engineering
in Partial Fulfillment of the Requirements for
the Degree of

Master of Science

in

Biomedical Sciences and Engineering

Koç University

January 23, 2015

Koç University

Graduate School of Sciences and Engineering

This is to certify that I have examined this copy of a master's thesis by

Serhat Varolgüneş

and have found that it is complete and satisfactory in all respects,

and that any and all revisions required by the final

examining committee have been made.

Committee Members:

_____

Prof. Alper Demir (Advisor)

_____

Prof. İlknur Tuğal Tutkun

_____

Prof. Ahmet Gül

Date: _____

To my family

ABSTRACT

In the presence of vitreous haze due to uveitis, fundus details become less discernible in fundus photography. Ophthalmologists use fundus photographs in order to evaluate the vitreous haze level of patients as an indication of the severity of the inflammation in the uveal tract. Manual inspection of fundus photographs is time consuming, in addition to being error prone. In this thesis, we propose an algorithmic methodology for automated photographic grading of vitreous haze. The proposed algorithm is founded on automatic quality assessment and fundus image segmentation techniques. The method has two stages, namely feature set extraction and classification. Several classifiers are trained using a data set of fundus images with varying degrees of vitreous haze. Promising results are presented based on a comprehensive set of extracted features and a support vector machine based classifier with a linear kernel function.

ÖZETÇE

Uveite bağlı vitröz bulanıklık, fundus fotoğrafında göz fundusunun ayrıntılarının seçilmesini zorlaştırır. Oftalmologlar fundus fotoğrafına bakarak, hastaların uveal ağındaki enflamasyonun şiddetinin bir göstergesi olarak, vitröz bulanıklık derecesini tespit ederler. Fundus fotoğraflarının manuel incelenmesi hem zaman kaybına yol açar hem de hatalara açıktır. Bu tezde, vitröz bulanıklığın otomatik fotoğrafik derecelendirilmesi için algoritmik bir metot öneriyoruz. Metodumuz iki kısımdan oluşmaktadır: öznitelik seti bulma ve sınıflandırma. Çeşitli sınıflandırma algoritmaları farklı derecede vitröz bulanıklığa sahip fundus resimleri ile eğitilmiştir. Doğrusal çekirdek fonksiyonuna sahip bir destek vektör makinesi ile sınıflandırılan kapsamlı bir öznitelik setinin sonuçları gösterilmiştir.

ACKNOWLEDGMENTS

Foremost, I would like to express my sincere gratitude to my advisor Prof. Alper Demir for the continuous support of my M.S. study and research, for his patience, motivation, enthusiasm, and immense knowledge. His guidance helped me in all the steps of my research and writing of this thesis.

I would like to thank also the rest of my thesis committee: Prof. İlknur Tuğal Tutkun and Prof. Ahmet Gül for their encouragement and insightful comments. I am very grateful to Prof. İlknur Tuğal Tutkun for providing the data set and grading it.

I thank my friends Deniz Kılınç, Bahadır Saltık, Haydar Ali Şeker, Tufan Kesen, and Burak Şeker for the stimulating discussions and all the fun we have had.

I would like to thank my parents Burhanettin and Dilmayi Varolgüneş and my sister Buşra and my brother Kendal Varolgüneş, for enduring this long process with me, always offering unequivocal support and love.

Last, but not least, I would like to thank Yasemin Bozkurt for her understanding and love. Her support and encouragement was in the end what made this thesis possible.

TABLE OF CONTENTS

LIST OF FIGURES

ABBREVIATIONS

AQA	Automatic Quality Assessment
BPO	Binary Path Opening
DR	Diabetic Retinopathy
FP	Fundus Photography
MD	Manually Designed Classifier
MDC	Morphological Degradation Covariance
MF	Matched Filter
MM	Mathematical Morphology
OD	Optic Disc
RBV	Retinal Blood Vessel
RV	Retinal Vasculature
SVM	Support Vector Machine

Chapter 1

INTRODUCTION

1.1 Problem Definiton

The aim of this work is to develop a solution to the problem of automated grading of vitreous haze. Currently, the vitreous haze levels of patients with uveitis are determined subjectively by ophthalmologists. Manual inspection consumes valuable time of medical staff and increases the chance of errors in diagnosis. A reliable algorithm would save both time and provide reproducible results.

1.2 Materials

Fundus photographic archives of the Uveitis Service at the Department of Ophthalmology, Istanbul University, Istanbul Faculty of Medicine, provided by Prof. Dr. İlknur Tuğal Tutkun, were used for the purpose of this study. All photographs had been taken using a standardized protocol that included patients' informed consent and were used in accordance with Declaration of Helsinki guidelines. Color fundus photographs showing the posterior pole at 50-degree field of view were acquired using a digital camera (Carl Zeiss Meditec, Hennigsdorf, Germany) after maximum pupil dilation.

İstanbul University, İstanbul Faculty of Medicine Ethics Committee approved the project.

1.3 Thesis Outline

Chapter 2 provides the ophtalmological background. The eye structure is briefly explained. Uveitis and vitreous haze are introduced. Diagnostic imaging techniques are listed and fundus photography and its use in vitreous haze scoring are summarized. Chapter 3 presents the algorithms that will be used in automated scoring of vitreous haze. Preprocessing, automatic quality assessment, and retinal blood vessel extraction algorithms are given. Algorithms to find a feature set and classification algorithms are provided with methods to assess the success of these algorithms in Chapter 4. The results of the algorithms are demonstrated in Chapter 5. Chapter 6 concludes the thesis with a summary and possible future research directions.

Chapter 2

OPHTALMOLOGICAL BACKGROUND INFORMATION

2.1 Eye Structure, Uvea and Fundus

The following information is retrieved from [1], [2], [3], [4], and [5].

The eye is the visual sensory organ and the human eye is an imperfect spherical structure. The wall of the eyeball is made up of three coats, or tunics, from outermost to innermost: fibrous (corneoscleral) tunic, vascular tunic (or uvea), and the sensory (nervous) tunic (or retina).

Fibrous tunic of the bulb of the eye is composed of dense, nearly-avascular connective tissue and divided into an anterior transparent cornea, a posterior sclera and the conjunctiva. ***The cornea*** is the dome-shaped anterior, transparent part of the eye. It is the chief refractive apparatus of the eye. ***The sclera*** (sclera = hard) is the white outer layer of the eye in humans. It is opaque and protective part of fibrous tunic, containing collagen and elastic fibers. ***The conjunctiva*** is a thin mucosal membrane covering the inner surface of the eyelid and the sclera. Being composed of cornea, sclera and conjunctiva, the fibrous tunic provides structure and protects the inner parts.

Vascular tunic, also called **uvea**, contains the iris, ciliary body and choroid. It is a pigmented layer and has blood vessels. ***The iris***, visible colored part of the eye, is the most anterior, heavily pigmented portion of the vascular layer. The iris regulates the amount of light entering the eye by adjusting the diameter of the pupil, the hole through which light passes. ***The ciliary body*** is a ring-shaped tissue which holds and controls the movement of the eye lens via ligaments, and thus, it helps to control the shape of the lens. ***The choroid*** lies between the retina and the sclera, and serves as the main source of blood supply for the photoreceptors of the retina due to the rich capillary content. The main roles of the uvea are nutrition and gas exchange and light absorption. The uvea provides the eye with blood supply and improves the contrast of the retinal image by reducing reflected light

within the eye.

The retina, the innermost of the three tunics of the eye where the images are received. Its outer surface is in contact with the choroid; its inner with the vitreous body. The retina contains photoreceptors (rods and cones) in the deepest layer which convert light into chemical and electrical signals.

Inside these three layers, exist the lens, the aqueous humour, and the vitreous body (humour). **The lens** is a biconvex, transparent, flexible structure, placed behind the pupil. Along with the cornea, it helps to refract light. **Aqueous humour** is a clear, watery fluid that is contained in two areas: anterior chamber (between the cornea and the iris), and posterior chamber (between the iris and the lens). **Vitreous body** is a gel-like structure that fills the the space between lens and the retina which makes up about 80% of the volume of eye. It allows light transmission through the eye, protects the retina, and supports the posterior surface of the lens and holds the neural layer of the retina firmly against the pigmented layer.

Fundus of a hollow organ is defined as the part farthest from its opening. Uterus, stomach, urinary bladder and eye have parts named fundus. The pupil is regarded as the opening when defining fundus of eye. It is the visible surface of the eye when looked through the pupil. The fundus of eye can be examined by ophthalmoscopy and/or fundus photography. Retinal vasculature, optic disc, macula and retinal background are visible in the fundus of a healthy person.

2.2 Imaging Modalities of Eye

Eye diseases and disorders, as well as several systemic diseases and disorders, manifest themselves on the visible parts of the eye; therefore, imaging the eye has been crucial for diagnostic purposes. Eye imaging allows ophthalmologists to assess and quantify ocular changes from a healthy condition [6]. Various imaging modalities have been developed to examine the eye structurally and/or functionally, including computer tomography (CT), optical coherence tomography (OCT), magnetic resonance imaging (MRI), ultrasound imaging, infrared thermography (IRT) [7], hyperspectral imaging [8], color Doppler imaging [9], photoacoustic ophthalmoscopy [10], blood-flow magnetic

resonance imaging [11], scanning laser ophthalmoscopy (SLO), confocal scanning laser ophthalmoscopy (cSLO) [12], fluorescein angiography (FA), autofluorescein angiography, color fundus photography (FP), red-free fundus photography, and stereo fundus photography. Some of these modalities such as FP, FA, SLO, cSLO, and IRT gather 2D data, whereas other modalities such as CT, MRI and OCT work on 3D data. Among the available imaging modalities, this thesis will focus on the color fundus photography technique.

2.2.1 Fundus Photography as a Diagnostic Tool

Fundus photography (FP) is a technique using a fundus camera specifically designed to picture the fundus of the eye. FP provides 2D structural information about the fundus. In the literature, FP is used to diagnose glaucoma [13], diabetic retinopathies (DR) [14], age-related macular degeneration, retinopathy of prematurity and vitreous haze [15].

2.3 Uveitis and Vitreous Haze

In most general terms, **uveitis** is the inflammation of the uvea. Anatomically, uveitis is divided into four classes: anterior uveitis, intermediate uveitis, posterior uveitis and pan-uveitis. Uveitis can be due to infectious or non-infectious (autoimmune) causes. Vitreous haze is one of the syndromes caused by uveitis types other than anterior uveitis.

Vitreous haze is the medical condition created by vitreous cells and exuding protein into vitreous body due to inflammation [16]. In presence of vitreous haze, fundus details become obliterated when viewed from ophthalmoscope or fundus photography.

2.4 Scale for Grading Vitreous Haze

Vitreous haze is graded by ophthalmologists to diagnose severity of inflammation and keep track of disease prognosis. Initially, a 5-step grade scale was proposed by Kimura et al. [17] based on the

clarity of the fundus through an ophthalmoscope. Later, Nussenblatt et al. [15] introduced their 6-step grade scale using fundus photographs. Their grade scale is based on the visibility of the fundus parts including the optic nerve head, retinal vessels, and nerve fiber layer [16]. The Nusenblatt scale is accepted by FDA for clinical use. The disadvantages of these grade scales include the following [16]:

- Grades do not correspond to measurable or quantifiable physical properties of fundus images.
- These scales have poor discrimination in small amounts of vitreous haze.
- These scales are not validated.

Davis et al. [16], propose a 9-level scale by using different Bangerter occlusion filters. The filters create optical blur similar to the one created by vitreous haze. Their grade scale is quantifiable, reproducible and validated.

In this thesis, a 5-step grade scale that is based on fundus image clarity is used to score images in the data set.

Chapter 3

FUNDUS IMAGE PROCESSING TOOLSET

3.1 Preprocessing

In the literature, preprocessing mainly includes the following tasks:

- Channel selection/inversion
- Field of view extraction
- Noise removal/smoothing
- Illumination correction
- Contrast normalization

3.1.1 Channel Selection/Inversion

The green channel, virtually always, is selected for further processing since it has the best contrast and clarity. The red channel blends blood vessels into the retinal background, though it has the widest histogram. The blue channel has the narrowest histogram and is very dark. Histograms of channels of a fundus image is given in Figure 3.1. The green channel can be inverted (the green image is subtracted from maximum pixel value) before processing to make the vessel pixels brighter than the background pixels for some applications.

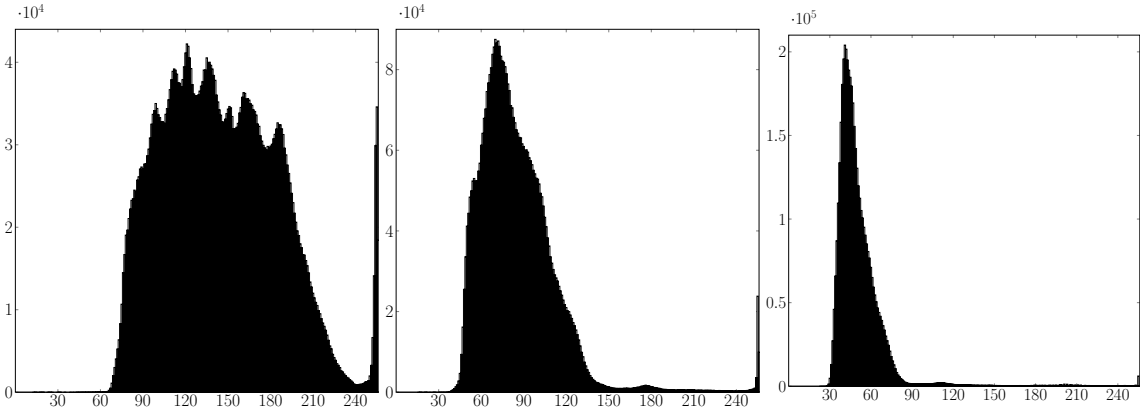

(a) Red (b) Green (c) Blue

Figure 3.1: Fundus Image with Channels

3.1.2 Field of View Extraction

Fundus images consist of a circular field of view (FOV) and a dark background. Excluding background pixels, when calculating features, reduces the required number of operations and eliminates noise-only component coming from background pixels. A binary mask, called FOV mask I_{FoV}, is generated for these purposes. I_{FoV} is used to restrict computations regarding fundus image into a field of interest.

Generally, for the same setup (camera and its settings), FOV does not change from image to image. Therefore, calculating the FOV mask once is sufficient while the system settings are kept the same. The data set used in this thesis is obtained from single source with relatively constant FOV.

The FOV mask, I_{FoV}, is defined, by using an average of whole data set I_{avg}, as follows:
$I_{FoV} = I_{avg} > 0.2$.
Finally, I_{FoV} is eroded with a disk structuring element of 15 pixels-radius to eliminate border irregularities encountered in fundus images by excluding pixels neighboring borders of FOV.

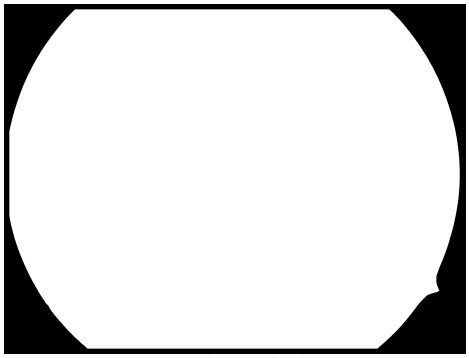

Figure 3.2: Field of View Mask

3.1.3 Noise Removal/Smoothing

Images obtained by digital cameras contain noise coming from several sources. Prior to any operation, these noise components should be eliminated from the image. The following algorithms can be utilized for noise removal: average smoothing, Gaussian smoothing, median filtering, anisotropic diffusion. There is a trade off of losing edge information when removing noise. As can be seen in Figure 3.3, median filter and anisotropic diffusion methods are the best ones in preserving important information when clearing the noise out. However, median filters remove objects smaller than their window sizes.

(a) Noisy (b) Average (c) Gaussian (d) Median (e) Anisotropic

Figure 3.3: Noise Removal Techniques

3.1.3.1 Anisotropic Diffusion Filter

Anisotropic diffusion filter is proposed by Perona & Malik [18]. The Gaussian filtering with a kernel of variance t, is taken as the solution of the following diffusion equation at time t with original images as the initial condition.

$$\begin{aligned} I(x,y,t) &= I_0(x,y) * G(x,y;t) \\ I_t &= c \cdot \Delta I = c \cdot (I_{xx} + I_{yy}) \end{aligned} \tag{3.1}$$

Instead of taking c constant everywhere in image, anisotropic diffusion reduces the diffusion rate, c, where gradient of image is high. The dependence of diffusion rate, c, on gradient of I is represented by two different functions, $c(x,y,t) = e^{-(\frac{\|\Delta I\|}{\kappa})^2}$ and $c(x,y,t) = \frac{1}{1+(\frac{\|\Delta I\|}{\kappa})^2}$, in [18]. As $\|\Delta I\|$ increases, diffusion rate gets smaller, thus high gradient (edge) pixels are not blurred by diffusion process, while noisy background pixels are smoothed out.

$$I_t = div(c(x,y,t) \cdot \nabla I) = c\Delta I + \Delta c \Delta I, \; where \, c(x,y,t) = g(\|\Delta I(x,y,t)\|) \tag{3.2}$$

Δ is Laplacian, div is divergence and ∇ is gradient operators.

Equation 3.2 is discretized using 4-nearest-neighbors discretization of the Laplacian operator as follows:

$$I_{i,j}^{t+1} = I_{i,j}^{t} + \lambda[c_N \cdot \nabla_N I + c_S \cdot \nabla_S I + c_E \cdot \nabla_E I + c_W \cdot \nabla_W I]_{i,j}^{t} \tag{3.3}$$

$$\begin{aligned}
\nabla_N I^t_{i,j} &= I^t_{i-1,j} - I^t_{i,j},\ c^t_{N_{i,j}} = g(|\Delta_N I^t_{i,j}|) \\
\nabla_S I^t_{i,j} &= I^t_{i+1,j} - I^t_{i,j},\ c^t_{S_{i,j}} = g(|\Delta_S I^t_{i,j}|) \\
\nabla_E I^t_{i,j} &= I^t_{i,j-1} - I^t_{i,j},\ c^t_{E_{i,j}} = g(|\Delta_E I^t_{i,j}|) \\
\nabla_W I^t_{i,j} &= I^t_{i,j+1} - I^t_{i,j},\ c^t_{W_{i,j}} = g(|\Delta_W I^t_{i,j}|)
\end{aligned} \tag{3.4}$$

Finally, at each time step t, $c^t_{N_{i,j}}$ and $\nabla_N I^t_{i,j}$ are calculated using Equation 3.4. Then, the calculated values are used to find the image at the next time step $I^{t+1}_{i,j}$ according to Equation 3.3. λ parameter is the time step size and it affects the amount of diffusion each step creates. κ parameter acts as a threshold that discriminates the edge pixels from the background pixels and is selected according to the noise levels. After selecting parameters, amount of smoothing can be adjusted by changing number of iterations.

3.1.4 Illumination Correction

Existence of glares in image borders, and over- and under-exposed regions in fundus images reduces the accuracy of automatic quality assessment and vessel segmentation algorithms. Therefore, an illumination correction algorithm should be utilized as a preprocessing step when algorithms that are sensitive to nonuniform illumination are used. There are several ways to compensate nonuniform illumination, some of which are explained below.

Running average window: Each pixel value is divided by the average value over a window located on that pixel.

Morphological illumination correction: Each pixel value is divided by the corresponding pixel value in the morphologically closed version of the original image. Closing is applied with a disk structuring element of 50 pixels radius (at least 25 pixels radius should be used since widest vessels (dark objects) are 25 pixels wide).

Chernomorets et al. [19] method: Firstly Mahalonobis distance, D, for each pixel, (x, y), is cal-

culated in Equation 3.5 to identify background pixels using the mean, $\mu(x, y)$, and the standard deviation, $\sigma(x, y)$, of all pixels in a window located at (x, y). Then, the pixel is classified as a background pixel if $D(x, y) < D_T$. The corrected intensity value, $I_C(x, y)$, is calculated in Equation 3.6 by using the mean, $\mu_B(x, y)$, and the standard deviation, $\sigma_B(x, y)$, of the background pixels in the same window located at (x, y).

$$D(x, y) = \left| \frac{I(x, y) - \mu(x, y)}{\sigma(x, y) + \sigma_\epsilon} \right| \tag{3.5}$$

$$I_C(x, y) = \left| \frac{I(x, y) - \mu_B(x, y)}{\sigma_B(x, y) + \sigma_\epsilon} \right| \tag{3.6}$$

A small σ_ϵ is used to avoid division by zero.

3.1.5 Contrast Normalization

Good contrast is crucial for proper functioning of the most of the vessel extraction algorithms. Contrast normalization can be achieved by using ordinary histogram equalization (HE) or contrast limitied adaptive histogram equalization (CLAHE) [20].

3.2 Segmentation of Fundus Image Parts

3.2.1 Segmentation of Optic Disc and Macula

Optic disc (OD) is the brightest region in a fundus image. Although there are various methods for extracting optic disc, a simple thresholding method will be used to detect center of the OD.

Fovea detection methods are based mainly on two properties of the fovea which are:

1. Fovea is a round area which is darker than its surroundings.
2. Fovea center is located at approximately 2.5 optic disc (OD) diameters from the OD center.

Location of fovea is determined chiefly using these illumination (1) and anatomical position properties (2).

Sinthanayothin et al. [21] consider the fovea as the darkest area in the fundus image. Intensity of fovea and blood vessels are taken as the same. Maximum correlation response to template intensities (almost a typical fovea) is assumed to be obtained from the location of the fovea. The location is further checked if the requirement (2) is satisfied or not.

After generation of a coarse resolution image from the original image, Gagnon et al. [22] select the darkest pixel that satisfies (2). Then, on the original image, fovea center is searched nearby of this darkest pixel.

Lie et al.' [23] method uses vascular arch to decrease the search area, in addition to (1) and (2). To extract the main course of the vasculature based on OD location, an active shape model is employed. According to this model and (2), a region of interest is obtained. In that region, center of the fovea is found by applying a thresholding scheme.

Niemeijer et al.'s [24] method models the distribution of all retinal features. To fit a point distribution model to the fundus image, they utilize an optimization method. This fitting process results in determination of the location of the normal anatomy. As a further work in [25], after finding the OD and its location, a region of interest for the fovea is specified. Within this region, the location with the lowest predicted distance to the fovea is taken as the location of fovea.

In this thesis, a simple thresholding approach with morphological closing operation is used to find macula.

3.2.2 Retinal Blood Vessel Segmentation

Retinal vasculature (RV), as uveal circulation, is a part of the blood supply system of the eye, and composed of the arteries, veins and their tributaries. Its role is to supply the inner layer of the retina. RV, with the optic nerve, arrives the retina perpendicularly at the optic disc. From there, the central artery and vein of RV bifurcates several times to cover retinal surface. RV is visible in

fundus images. The vessels in fundus images, appear darker than the retinal surface background due to their low reflectance.

Accurate detection of retinal blood vessels (RBVs) provides essential information in the identification of ophthalmologic conditions. RBV changes can be detected and quantified using RBV segmentation algorithms to aid diagnosis and treatment of several diseases, therefore, RBV segmentation has been a widely studied field of interest. The literature for RBV segmentation methods is vast, hence I will only summarize the main ideas and prominent methods and then explain algorithms that I use in this thesis.

Conceptually, RBV segmentation methods can be classified into the following groups:

- Filtering/Matched filtering
- Vessel tracking
- Morphological processing
- Supervised learning/Pixel-based classification
- Other Methods

Various studies combine these approaches into one algorithm, therefore can be classified as a member of more than one group.

3.2.3 Matched Filtering

Matched filtering (or matched filter, MF) is used to find a desired pattern, signal component or feature in a signal. The MF kernel is the template of the feature. Filter response is high at the places where the searched pattern is present in the input signal. For example, if a sinusoidal pattern is sought in a 1D signal, a matched filter template of sinusoidal pattern gives the highest response to that pattern in the whole input signal.

In their work [26], Chaudhuri et al. proposed the use of MF for RBV enhancement as a first step in extraction of RBV pixels by adaptive thresholding. Profile of their two-dimensional linear kernel

is designed to match that of the RBVs, as can be seen in Figure 3.4. Their template is based on the following three properties of the RBVs in fundus images:

1. RBVs have little curvatures, therefore, vessels can be approximated by piecewise linear segments.
2. The intensity profile of RBV cross-section resembles a Gaussian curve.
3. Diameter of the vessels decrease gradually as vessels move further from optic disc.

So, filters have a Gaussian profile, they are extruded longitudinally and several Gaussian curves with varying standard deviations (modeling vessel width) are used. Moreover, vessels can be in any position and orientation, therefore, several rotated versions (with 30° steps) of the MF are convolved with the input image.

$$K(x,y) = -exp(-x^2/2\sigma^2) \qquad for\,|y| \leq L/2 \tag{3.7}$$

Different orientations are obtained by rotating the coordinates, x & y, by angle θ:

$x' = cos(\theta)x + sin(\theta)y$, & $y' = -sin(\theta)x + cos(\theta)y$.

K is ensured to be zero mean by subtracting mean of K from itself.

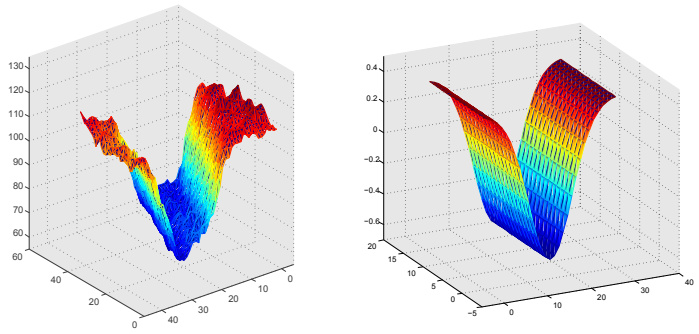

(a) Vessel Profile (b) Template Profile

Figure 3.4: Vessel Profile and Matched Filter Template

Bifurcations, tortuous vessels, and vessels with central reflex cause incorrect MF results.

Algorithm 1 Matched filtering RBV segmentation

function MATCHEDFILTERING($I, \sigma_{min}, \sigma_{step}, \sigma_{max}, \theta_{step}, L$)
    Given values α, U_E
    for $\sigma = \sigma_{min}\, to\, \sigma_{max} : \sigma_{step}$ **do**
        for $\theta = 0\, to\, \pi - \theta_{step} : \theta_{step}$ **do**
            $I_{\sigma,\theta}(x, y) = I(x, y) * K_{\sigma,\theta,L}(x, y)$
        end for
    end for
    $I_{MF}(x, y) = \max_{\sigma,\theta} I_{\sigma,\theta}(x, y)$
end function

3.2.4 Vessel Tracking

Vessel tracking methods use an initial set of seed points to track vessels starting from these points, thus the initial set should be guaranteed to be on the RV. Tracking is based on the local information at the level of a single vessel. None of these methods is implemented in this work.

3.2.5 Mathematical Morphology

Mathematical morphology (MM) based methods use the known morphology of the RV which consists of connected piecewise linear segments. Basic morphological operators (erosion, dilation, opening, closing, top-hat, reconstruction, etc.) and more advance morphological operators are utilized to extract RBVs. Mathematical morphology provides RBV segmentation task with speed and noise resistance.

3.2.5.1 Method of Zana & Klein

Zana & Klein [27] propose a method using MM and curvature evaluation together. They use inverted green channel, S_0, to process, so that the vessels become brighter than the retinal background. Firstly, they find the supremum of the linear openings (S_{op}) of the original image (S_0) for 15 pixels long line structuring elements (L_i) with 12 different angles. In this thesis, linear structuring elements will be 25 pixels long, considering the width of the widest vessels. Linear openings will erase bright

structures that line elements can not be placed in. Taking supremum will save bright structures that at least one of the structuring elements with different angles can be placed in. By this way, when summing top-hats for the linear openings, only the vessels will be enhanced among other bright regions which are circular and small regions caused by diseases or noise. Vessels can be segmented with a threshold using S_{sum}, but further processing the S_{sum} by finding its curvature help ensuring that the noise is eliminated. Laplacian of Gaussian of S_{sum}, S_{lap}, is found and its linear opening by reconstruction, S_1, is calculated. Using the alternating filters (linear opening by reconstruction, linear closing by reconstruction) and thresholding S_{res} is calculated.

$$\begin{aligned} S_{op} &:= \gamma^{rec}_{S_0}(\max_i\{\gamma_{L_i}(S_0)\}) \\ S_{sum} &:= \sum_{i=1}^{12}(S_{op} - \gamma_{L_i}(S_0)) \\ S_{lap} &:= Laplacian(Gaussian^{width=7px}_{\sigma=7/4}(S_{sum})) \\ S_1 &:= \gamma^{rec}_{S_{lap}}(\max_i\{\gamma_{L_i}(S_{lap})\}) \\ S_2 &:= \phi^{rec}_{S_1}(\min_i\{\phi_{L_i}(S_1)\}) \\ S_{res} &:= \max_i\{\gamma^2_{L_i}(S_2)\} \geq 1 \end{aligned} \tag{3.8}$$

3.2.5.2 Path Openings and Closings

Heijmans et al. [28] proposes a new advanced morphological method for processing paths, namely, binary path openings (BPOs). Traditional filtering for linear structures in images uses the union of openings by straight lines. In general, paths are curved. Path opening is done by using every possible path with a specific length as structuring element and taking the supremum of the openings.

Specifity of the segmentation methods can be increased by using BPOs to exclude short and unoriented patches of noise that are segmented as vessels.

Although their method is generalized to grayscale images as well, it is left unimplemented.

3.2.6 Supervised Classification

Supervised classification methods compute a feature vector for each pixel in the training image set using local or global information. Then, a supervised classifier is trained using the ground truth data (training image set with manually labeled retinal vasculature). A new input image is processed by first computing a feature vector for its pixels and then classifying its pixels either as vessel or background using the trained classifier. Methods in this group differ according to how the feature vector is computed and which classifier is used.

3.2.6.1 Gabor Wavelet Transform

Soares et al. [29] use Gabor wavelet transform to construct the feature vector. The feature vector for each pixel is composed of the pixel's intensity and its Gabor wavelet transform responses. They use "a Bayesian classifier with class-conditional probability density functions (likelihoods) described as Gaussian mixtures" [29]. General 2D Gabor filter is defined in Equation 3.9 [30].

"The filter is centered at $(x = x_0, y = y_0)$ in the spatial domain, and at $(\xi = \xi_0, \nu = \nu_0)$ in the spatial frequency domain. σ and β are the standard deviations of an elliptical Gaussian along the x and y axes. θ is the orientation of the filter, rotated counter-clockwise around the origin. ρ is the absolute phase of an individual filter" [30].

$$\psi(x, y, \xi_0, \nu_0, x_0, y_0, \rho, \theta, \sigma, \beta) = \frac{1}{\sqrt{\pi\sigma\beta}} \cdot e^{-\left(\frac{((x-x_0)cos\theta + (y-y_0)sin\theta)^2}{2\sigma^2} + \frac{(-(x-x_0)sin\theta + (y-y_0)cos\theta)^2}{2\beta^2}\right)} \cdot e^{i(\xi_0(x-x_0)+\nu_0(y-y_0)+\rho)} \tag{3.9}$$

This complex definition can be simplified using a few substitutions. The coordinates can be changed as $x' = (x - x_0)cos\theta + (y - y_0)sin\theta$ and $y' = -(x - x_0)sin\theta + (y - y_0)cos\theta$. Constraining $\xi_0 = \omega_0 cos\theta$ and $\nu_0 = \omega_0 sin\theta$ and defining $\gamma = \sigma/\beta$ simplify the equation as follows:

$$\psi(x', y', \omega_0, \rho, \sigma, \gamma) = \frac{1}{\sqrt{\pi\gamma}\sigma} e^{-\left(\frac{x'^2 + \gamma^2 y'^2}{2\sigma^2}\right)} \cdot e^{i(\omega_0 x' + \rho)} \tag{3.10}$$

With the simplified expression, it is easier to see that θ is orientation of the filter; γ gives elongation to the filter; σ is spread of the filter; ω_0 is the spatial frequency of the filter.

In Soares et al. [29], 2D Gabor wavelet is defined as (using $\gamma = 0.5$, $\rho = 0$, and σ & θ embedded into vector coordinates x):

$$\begin{gathered} \psi_G(x) = exp(jk_0 x) exp\left(-\frac{1}{2}|Ax|^2\right) \\ k_0 = [0, 3], A = diag[2, 1] \end{gathered} \tag{3.11}$$

They scale and rotate coordinate x to get wavelet set $\psi_{b,\theta,a}$ with translations b, rotations θ, and scalings a. They use θ range from 0° to 170° using 10° steps, and take maximum value of these $\psi_{b,\theta,a}$ filtering results to get $\psi_{b,a}$ at each scale.

3.3 Automatic Quality Assessment

As mentioned in Section 2.2.1, fundus imaging is frequently used by medical specialists for manual, computer aided or automatic diagnosis. The fundus image quality may be inadequate due to the photographers skills and experience, the equipment properties, and the patient. Moreover, eye property variations among individuals introduce quality differences in FP. Reliable diagnosis depends on sufficient image quality. A poor quality FP is misleading for manual diagnosis. Moreover, automated processing techniques can not give correct results for a poor quality FP. Quality of fundus images should be verified during acquisition, since a reacquisition for the poor quality image will be time consuming.

Several automatic quality evaluation methods were developed for objective and quantitative verification of the diagnostic adequateness of the images. These methods identify over- and underexposed, unfocused, non-uniformly illuminated, and noisy images. Image properties such as blurri-

ness, sharpness, contrast, brightness, noise levels, and clarity of image contents are used to evaluate quality. Vitreous haze creates deteriorations in images similar to the ones quantified by automatic quality assessment (AQA) methods; therefore, AQA methods can be used to quantify vitreous haze amount. Note that, when used to quantify vitreous haze levels, fundus images should be taken with the best possible quality, since poor quality will cause overestimated vitreous haze scores.

3.3.1 Histogram Based Methods

Histogram based methods were the first attempts to solve AQA problem for fundus images. In [30], a reference histogram is compared with the input image histograms. The reference histogram is constructed using 20 excellent quality fundus images. The spread of the image intensity histogram is accepted as a measure of contrast in the image. Similarity of reference and input image histograms, found by convolving two histograms, defines quality metric, Q, of this method.

However, a later study found that the global intensity histogram similarity measure is not strongly correlated with image quality [31]. A refinement on this method is using global edge histogram with the local image intensity histogram [31]. Firstly, global edge histogram is computed using Sobel derivative of original input image.

$$k_x = \begin{bmatrix} 1 & 0 & -1 \\ 2 & 0 & -2 \\ 1 & 0 & -1 \end{bmatrix}, \; k_y = \begin{bmatrix} 1 & 2 & 1 \\ 0 & 0 & 0 \\ -1 & -2 & -1 \end{bmatrix} \tag{3.12}$$

$$G = \sqrt{I_x^2 + I_y^2}, \; where \, I_x = k_x * I, \; I_y = k_y * I. \tag{3.13}$$

A convolution with Sobel kernels, k_x and k_y, is a discrete form of derivatives in x and y directions. I is the input image and G is the Sobel derivative of the input image. The global edge histogram is actually the histogram of image G.

A reference histogram is used as a template as in [30]. The difference between two histograms is

measured using following χ^2 statistics like formula:

$$d_{edge}(T,R) = \sum_i \frac{(R_i - T_i)^2}{R_i + T_i}, \forall\, i \mid R_i + T_i \neq 0 \tag{3.14}$$

The edge magnitude histograms of high quality images are wider and as magnitude parameter increases, histogram values slowly drop in contrast to edge magnitude histograms of poor quality images which are narrow and drop sharply [31] as can be seen in Figure 3.5. Edge magnitude histogram similarity metric provides a measure of sharpness and proper focus. In addition to similarity metric, I will use mean and standard deviation of the edge magnitude histograms, and sum and mean of their tails as global quality features. Tails will be computed using a threshold, explained in detail in Section 3.3.3.2.

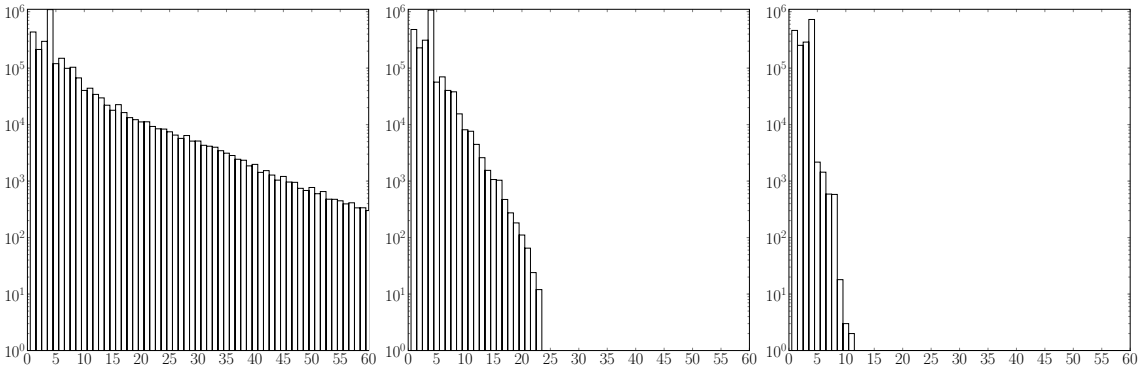

(a) Grade 0 (b) Grade 1 (c) Grade 3

Figure 3.5: Edge Magnitude Histograms

Secondly, the local image intensity distribution is used to evaluate quality of the fundus images. Good contrast and adequate illumination can be assessed by using image intensities. A set of reference images are aggregated to get I_{Mean}. Input image I_{Target} is segmented into uniform regions by a histogram-splitting method. The histograms of each of these regions are compared to the histogram of the corresponding regions of the reference image. W is the function that measures the distance between two histograms.

$$d_{intensity}(I_{Target}, I_{Mean}) = \sum_{i=1}^{N_b regions} Size_i \cdot W(HR_i^{(I_{Target})}, HR_i^{(I_{Mean})}) \tag{3.15}$$

3.3.1.1 Disadvantages of Histogram Based AQA Methods

Main drawbacks of histogram based methods are:

- Reference histogram model is constructed using a small set of images.
- (Results are) Susceptible to the natural variance found in retinal images.

3.3.2 Segmentation Based Methods

Clarity of image contents can be a good indicator of image quality. Retinal vasculature (RV), optic disc (OD) and macula visibility are prerequisites of diagnosis. Hence, segmentation of RV, OD and macula is the first step in defining clarity of image. One of the first studies to use RV extraction for AQA was Usher et al. [32]. In their method, detected vessel area is used as a metric to assess the quality. However, the total vessel area varies among individuals naturally, in addition to disease related variations. Instead of using vessel segmentation in whole image, Fleming et al. proposed measuring vessel density around the macula, where the thinnest vessels are located [33]. Since quality degradations initially alter the visibility of small vessels, measuring the thin vessels around the macula is a better approach. After detection of optic disc and macula, they segmentate vessels in 3.5 optic disc diameter around the center of the macula. RV, OD, and macula extraction methods are explained in Section 3.2.

3.3.2.1 Vessel Edge Width

Chernomorets and Krylov, use vessel segmentation to find vessel edge widths as a measure of blurriness of image [34]. After detection of vessels, they extract vessel profiles (cross sections) of

the largest width vessels. Using their general edge model, they identify 1D vessel profiles' edge widths.

The general edge, E_σ is modeled as the ideal unit step edge, $H(x)$, convolved with a Gaussian with dispersion σ, G_σ. The edge width of the general edge is taken to be the dispersion σ.

$$H(x) = \begin{cases} 1, & x \geq 0, \\ 0, & x < 0. \end{cases} \tag{3.16}$$

$$E_\sigma(x) = [H * G_\sigma](x) \tag{3.17}$$

For a given edge profile, the following equation holds:

$$E_\sigma(x) = E_{\sigma'}(\frac{\sigma'}{\sigma}x) \tag{3.18}$$

They use unsharp masking of edge profile as defined below:

$$U_{\sigma,\alpha}[E_{\sigma_0}](x) = (1+\alpha)E_{\sigma_0}(x) - \alpha E_{\sigma_0} * G_\sigma = (1+\alpha)E_{\sigma_0}(x) - \alpha E_{\sqrt{\sigma_0^2+\sigma^2}}(x) \tag{3.19}$$

for $\sigma = \sigma_0 = \sigma_1$

$$\begin{aligned} U_{\sigma_1,\alpha}[E_{\sigma_1}](x) &= (1+\alpha)E_{\sigma_1}(x) - \alpha E_{\sqrt{2}\sigma_1}(x) \\ &= (1+\alpha)E_{\sigma_2}(\frac{\sigma_2}{\sigma_1}x) - \alpha E_{\sqrt{2}\sigma_2}(\frac{\sqrt{2}\sigma_2}{\sqrt{2}\sigma_1}x) \\ &= U_{\sigma_2,\alpha}[E_{\sigma_2}](\frac{\sigma_2}{\sigma_1}x). \end{aligned} \tag{3.20}$$

The unsharp masking of E_σ for a given α, $U_{\sigma,\alpha}[E_{\sigma_0}](x)$, has the same extrema, x_{min_σ} and x_{max_σ}, for $\forall\sigma > 0$. Moreover, $U_{\sigma,\alpha}[E_{\sigma_0}](x)$ is an increasing function of parameter σ while $x > 0$.

$$U_E = \max_x U_{\sigma_E,\alpha}[E_{\sigma_E}](x) \, for \, some \, \sigma_E \tag{3.21}$$

Any input profile E_{σ_0}, will have $\max_x U_{\sigma_0,\alpha}[E_{\sigma_0}](x) = U_E$ due to Equation 3.20, hence:

$$\begin{aligned} &\max_x U_{\sigma,\alpha}[E_{\sigma_0}](x) \leq U_E, \; \sigma < \sigma_0 \\ &\max_x U_{\sigma,\alpha}[E_{\sigma_0}](x) \geq U_E, \; \sigma > \sigma_0. \end{aligned} \tag{3.22}$$

Algorithm 2 Edge width estimation

```
1:  function EDGEWIDTHESTIMATION(E_σ0)                    ▷ E_σ0 is a 1D profile
2:      Given values α, U_E
3:      for σ = σ_min to σ_max : σ_step do
4:          Compute U_σ,α[E_sigma0](x)
5:          Find local maxima x_maxσ of U_σ,α[E_sigma0](x)
6:          if U_σ,α[E_sigma0](x_maxσ) ≥ U_E then
7:              σ_estimated ← σ
8:              Stop cycle
9:          end if
10:     end for
11: end function
```

After finding the edge widths for the selected profiles, $10\frac{W_i}{A_i}$ value is calculated, where W_i is the estimated edge width and A_i is the amplitude of the edge for i^{th} profile. Median value of the calculated values is the resulting blur value estimation.

3.3.2.2 Elliptical Vessel Density

An improvement of vessel area measure is proposed by Giancardo et al. [35]. In their method, elliptical local vessel density metric based quality assessment, an ellipse is fitted to the fundus image and 18 local windows are defined with respect to the center and the radius, r_e, of the ellipse. Vessel density in each of these windows is computed, normalized and used as a part of the feature set. The windows are defined in polar coordinates as follows: $W_{i,j} = \{(r,\theta) \, | (i-1)\frac{r_e}{3} \leq r < i\frac{r_e}{3},$

$(j-1)\frac{\pi}{3} \leq \theta < j\frac{\pi}{3}, i \in \{1,2,3\}, j \in \{1,2,3,4,5,6\}\}$. Vessel segmentation is done using method of Zana et al. [27].

In order to accomplish AQA task, they combine elliptical local vessel density features with 5 bins histograms of the three color channels of the RGB image. The total 33 features used were to measure quality of the image with a classifier. Results are obtained using several classifiers.

3.3.2.3 Anisotropicity Metric

In order to find anisotropicity metric proposed by Kohler et al. [36], $M \times N$ input image, I, is divided into distinct patches, P, of size $n \times n$. The local gradient matrix, G, of size $n^2 \times 2$ is calculated for each P. Columns of G are vectorized forms of the first order derivative matrices of I in x and y directions. Then singular values of G, s_1 & s_2, are found using singular value decomposition (SVD) of G. Using s_1 & s_2, a local quality metric $q(P)$ is found for each patch P.

$$\begin{aligned} G =& \begin{bmatrix} P_x(1,1) & P_y(1,1) \\ \vdots & \vdots \\ P_x(n,n) & P_y(n,n) \end{bmatrix} \\ G =& UDV^T = U \begin{bmatrix} s_1 & 0 \\ 0 & s_2 \end{bmatrix} V^T \\ q(P) =& s_1 \cdot R, \; where\, R\, indicates\, coherence \\ R =& \frac{s_1 - s_2}{s_1 + s_2} \end{aligned} \tag{3.23}$$

The local quality metric $q(P)$ shows the image noise and blur in an anisotropic patch P. High $q(P)$ values represent higher image quality in terms of the amount of blur and noise in the image. For isotropic patches, $q(P)$ does not make sense. In anisotropic patches with dominant gradient direction, $q(P)$ is a global estimate for blur and noise. Therefore, the quality metric, Q is found by summing and normalizing $q(P)$ values for all anisotropic patches.

$$Q = \frac{1}{MN} \sum_{i,j:P(i,j)=1} q(P_{ij}) \tag{3.24}$$

where $P(i,j)$ denotes the patch map for image I such that $P(i,j) = 1$ if $P(i,j)$ is anistropic.

Additionally, in [36], a vesselness measure for detection of blood vessels is used and a spatially weighted quality metric is calculated but not included in this thesis.

3.3.2.4 Disadvantages of Segmentation Based AQA Methods

Shortcomings of segmentation based methods are:

- The processing times are long due to initial segmentation step.
- Segmentation failure may occur due to factors other than low quality, including natural and disease-related variance.

3.3.3 Miscellaneous Methods

Gathering a feature set (for a pixel or the image) is the initial step of the methods presented in the current section. In this thesis, some of the features that are defined in these methods will be utilized as features to classify vitreous haze. Several studies perform a clustering on the feature set to reduce its dimension, before inputting it into the classifier.

3.3.3.1 Image Statistics Set

Mean, variance, skewness, kurtosis and higher order moments of the image histogram can be used as a feature set.

3.3.3.2 Sharpness Metrics

These correspond to the sum and mean of the tails of the edge magnitude historgrams identified in Section 3.3.1. Sobel derivative, or edge image, G is defined in Equation 3.13. Sharpness metrics are defined in [37] as:

$$\begin{aligned} s_1 &= \frac{\sum\limits_{i,j} G(i,j) \geq \alpha}{M \cdot N} \\ s_2 &= \frac{\sum\limits_{i,j} (G(i,j) \geq \alpha) \cdot G(i,j)}{s_1} \\ \alpha &= \frac{2 \sum\limits_{i,j} G(i,j)}{M \cdot N} \end{aligned} \tag{3.25}$$

s_1 and s_2 are the total count and mean intensity of the pixels with intensity values greater than the defined threshold. The threshold α is defined as twice the mean value of the edge image.

3.3.3.3 Haralick Texture Features

Haralick texture features, a total of 28, are developed to identify objects and regions using their textural properties [38]. In AQA field, Paulus et al. [37] were first to use Haralick texture features as generic criteria to assess quality of fundus images. They use entropy, energy, and contrast defined in [38], as measures of common image sharpness, homogeneity, and generic contrast, respectively [37]. These features are calculated using spatial-dependence (or co-occurence) matrices defined as:

$$
\begin{aligned}
P(i,j,d,0^\circ) &= \#\{((k,l),(m,n)) \in (L_y \times L_x) \times (L_y \times L_x) \,| \\
&\qquad k-m=0, |l-n|=d, \\
&\qquad I(k,l)=i, I(m,n)=j\} \\
P(i,j,d,45^\circ) &= \#\{((k,l),(m,n)) \in (L_y \times L_x) \times (L_y \times L_x) \,| \\
&\qquad (k-m=-d, l-n=d) \, or \, (k-m=d, l-n=-d), \\
&\qquad I(k,l)=i, I(m,n)=j\} \\
P(i,j,d,90^\circ) &= \#\{((k,l),(m,n)) \in (L_y \times L_x) \times (L_y \times L_x) \,| \\
&\qquad |k-m|=d, l-n=0, \\
&\qquad I(k,l)=i, I(m,n)=j\} \\
P(i,j,d,135^\circ) &= \#\{((k,l),(m,n)) \in (L_y \times L_x) \times (L_y \times L_x) \,| \\
&\qquad (k-m=d, l-n=d) \, or \, (k-m=-d, l-n=-d), \\
&\qquad I(k,l)=i, I(m,n)=j\}
\end{aligned}
\tag{3.26}
$$

The direction angle is parametrized as $r \in \{0^\circ, 45^\circ, 90^\circ, 135^\circ\}$. Distance-one spatial-dependence metrics are used to calculate the three features. Matrix entries are normalized with the total number of pixel pairs satisfying distance-one ($d = 1$) condition in each direction r.

$$
p(i,j,r) = \frac{P(i,j,r)}{N_r} \tag{3.27}
$$

$$
\begin{aligned}
Entropy : h_1 &= -\frac{1}{4} \sum_{i,j,r} p(i,j,r) log(p(i,j,r)) \\
Energy : h_2 &= \frac{1}{4} \sum_{i,j,r} p(i,j,r)^2 \\
Contrast : h_3 &= \frac{1}{4} \sum_{l}^{N_g-1} l^2 \left\{ \sum_{|i-j|=n} p(i,j,r) \right\}
\end{aligned}
\tag{3.28}
$$

3.3.3.4 Image Structure Clustering

Niemeijer et al. [39] represented image quality by utilizing two sets of feature; namely, color and second order image structure invariants (ISI). Measurement of color is done through the normalized histograms of the RGB planes, each of which contains 5 bins. In ISI, to generate features that are invariant to rotation, position or scale, filterbanks based on the gauge coordinate system are employed. Gauge coordinate system is a local coordinate system defined at each pixel with the gradient vector and a vector perpendicular to the gradient direction, as basis. Filterbank is composed first and second order derivatives of luminosity, L, in gauge coordinate system. The derivatives of luminosity are calculated by using Gaussian filters with 5 different standard deviations, $\sigma = 1, 2, 4, 8, 16$. Taking derivatives in gauge coordinate system makes ISI rotation independent and using Gaussians with different standard deviations provides ISI with scale invariance. After applying filterbank, a total of 25 filter responses for each pixel is obtained. Using randomly sampled 150 response vectors from 500 images, clusters or "visual words" are created. For each new image, ISI response vectors for every pixel is calculated and normalized vectors are clustered using k-means clustering. Histogram of the ISI "visual words" image for the input image is used as the second feature set. Gauge coordinate system and second order ISI filter definitions are given in Equations 3.29 and 3.30.

$$Gauge\,coordinates : (\vec{v}, \vec{w})\, where\, \vec{w} = (\frac{\delta L}{\delta x}, \frac{\delta L}{\delta y})\, and\, \vec{v} \perp \vec{w} \tag{3.29}$$

$$\begin{aligned} L_w =& \sqrt{L_x^2 + L_y^2} \\ L_{vv} =& \frac{-2L_xL_{xy}L_y + L_{xx}L_y^2 + L_x^2L_{yy}}{L_x^2 + L_y^2} \\ L_{vw} =& \frac{-L_x^2L_{xy} + L_y^2L_{xy} + L_xL_y(L_{xx} - L_{yy})}{L_x^2 + L_y^2} \\ L_{vv} =& \frac{L_x^2L_{xx} + 2L_xL_{xy}L_y + L_y^2L_{yy}}{L_x^2 + L_y^2} \end{aligned} \tag{3.30}$$

The two feature sets used to classify quality of image using several classifiers, and SVM with radial

basis kernel gave the best accuracy.

3.3.3.5 Morphological Degradation Covariance

Morphological degradation covariance metric is developed for this thesis, and is a novel technique. Vessel pixels in green channel are darker than their surroundings and for the image set used in this thesis, the widths of the widest vessels are about 25 pixels. So, a morphological closing operation with a structuring element of 25 pixel diameter disc will erase all vessels in the image. Taking covariance of the original image (or 5 pixel disc SE morphologically closed version) and the vessel-free image will give fine structure information content of the image.

Chapter 4

VITREOUS HAZE GRADING ALGORITHMS

Vitreous haze grading will be accomplished in two steps. The first step is calculating a feature set for the input image. The second step is assigning a vitreous haze grade to the feature set by a classifier. Sections 3.1-3.3 summarize preprocessing, segmentation, and automatic quality assessment algorithms. These algorithms constitute the basis for methods in Section 4.1, which are used to calculate the feature set. Section 4.2 presents the classification methods for the second step of automatic grading.

4.1 Features

Some of the algorithms explained in previous sections will be used in this section to create feature vector of the input image.

As a result, following feature set is obtained: μ, σ^2, s_1, s_2, μ_x, σ_x^2, s_{x_1}, s_{x_2}, x_{max}, h, Q, Z, A, W, B, d_{mac}, d_{min}, H_ϵ. First 12 features are calculated without extracting vessels. A, W, and B are the median amplitude, width and blur values calculated by edge width estimation algorithm explained in 3.3.2.1. d_{mac} is the vessel density in the macular region. d_{min} is the vessel density of the window with minimum vessel density. H_ϵ is elliptical vessel density histogram. Segmentation requiring features (A, W, B, d_{mac}, d_{min}, and H_ϵ) are not informative for images with moderate to heavy haze, therefore they are not included in the current work. They will be included after improving segmentation methods.

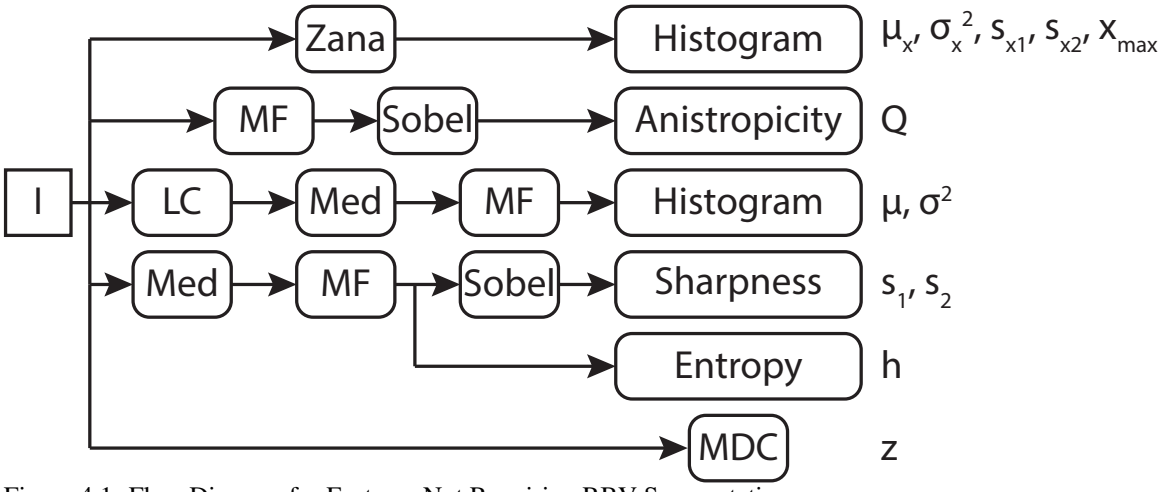

Figure 4.1: Flow Diagram for Features Not Requiring RBV Segmentation
Zana: Morphological processing based vessel extraction algorithm by Zana & Klein [27], MF: Matched filtering, Sobel: Sobel derivative, LC: Luminance correction by morphological closing, Med: Median filtering, MDC: Morphological degradation covariance

4.2 Classification

The data set contains limited number of images, therefore, splitting the data set into the training and test sets will further reduce the number of images used to train the classifier and will deteriorate the results of classification. However, testing the trained classifier with the same data set used to train it, will overestimate the success of the classification due to "testing hypotheses suggested by data" fallacy. "Testing hypotheses suggested by data" means that when a hypothesis is tested by the data that are used to construct it, test will pass even the hypothesis is wrong. In order to avoid both reducing training data set size and overestimating the results, leave-one-out cross-validation will be used. Each time the classifier will be trained by excluding one observation (image) and validated by the excluded observation.

Following classifiers are tested:

- Naive Bayes classifier (NB)
- Classification trees (CT)
- Support vector machines (SVM)

- Neural networks (NN)
- k-nearest neighbors (kNN)
- Generalized linear regression (GLM) with thresholding
- Manually designed classifier (MD)

A manually designed classifier is provided to prove that if simple thresholds on features (linear classification) classify images into grades with a particular accuracy, then, other methods can be successful with at least that accuracy without overfitting when the training sets are large enough.

Accuracy is the ratio of correctly classified images to the whole data set: $ACC = \frac{N_{correct}}{N_{dataset}}$.

4.2.1 Manually Designed Classifier

Manually designed (MD) classifier, uses two steps of simple thresholding of certain features. Structure is illustrated in Figure 4.2.

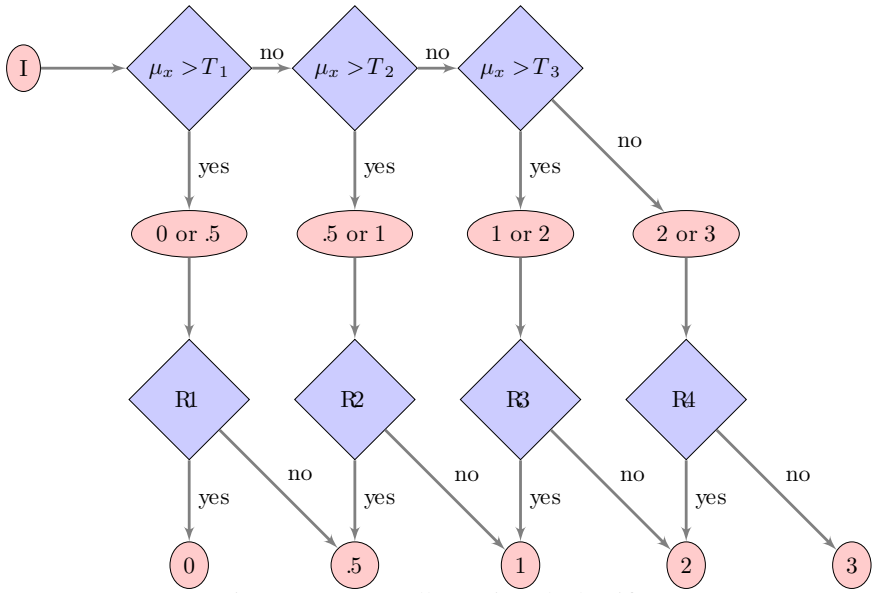

Figure 4.2: Manually Designed Classifier

The feature set of the input image is tested with conditions defined in Equation 4.1

$$
\begin{aligned}
R1 &= s_{x_1} > T_4 \,\&\, h > T_5 \\
R2 &= s_1 > T_6 \,\&\, s_2 > T_7 \\
R3 &= s_{x_1} > T_8 \,\&\, (s_1 > T_9 \,|\, (Q > T_{10} \,\&\, s_1 > T_{11} \,\&\, \mu_x > T_{12})) \\
R4 &= \mu_x > T_{13} \,\&\, h > T_{14} \,\&\, s_1 > T_{15}
\end{aligned}
\tag{4.1}
$$

The thresholds are selected to maximize accuracy of the classifier.

Chapter 5

RESULTS

Data set used in this thesis consists of 66 fundus images. For 5 grade steps (0, 0.5, 1, 2, 3), there are 8, 12, 15, 18, and 13 images, respectively. Images are graded by Prof. İlknur Tuğal Tutkun. Evaluation of automatic grading method will be based on this scoring.

5.1 Features

Normalized values for features grouped by grades are provided in Figure 5.1 with best possible classification results obtained by thresholding the feature. When combined, features are expected to improve these single feature classification results. Some features give somehow correlated results while others have distinct distributions as exemplified in Figure 5.2.

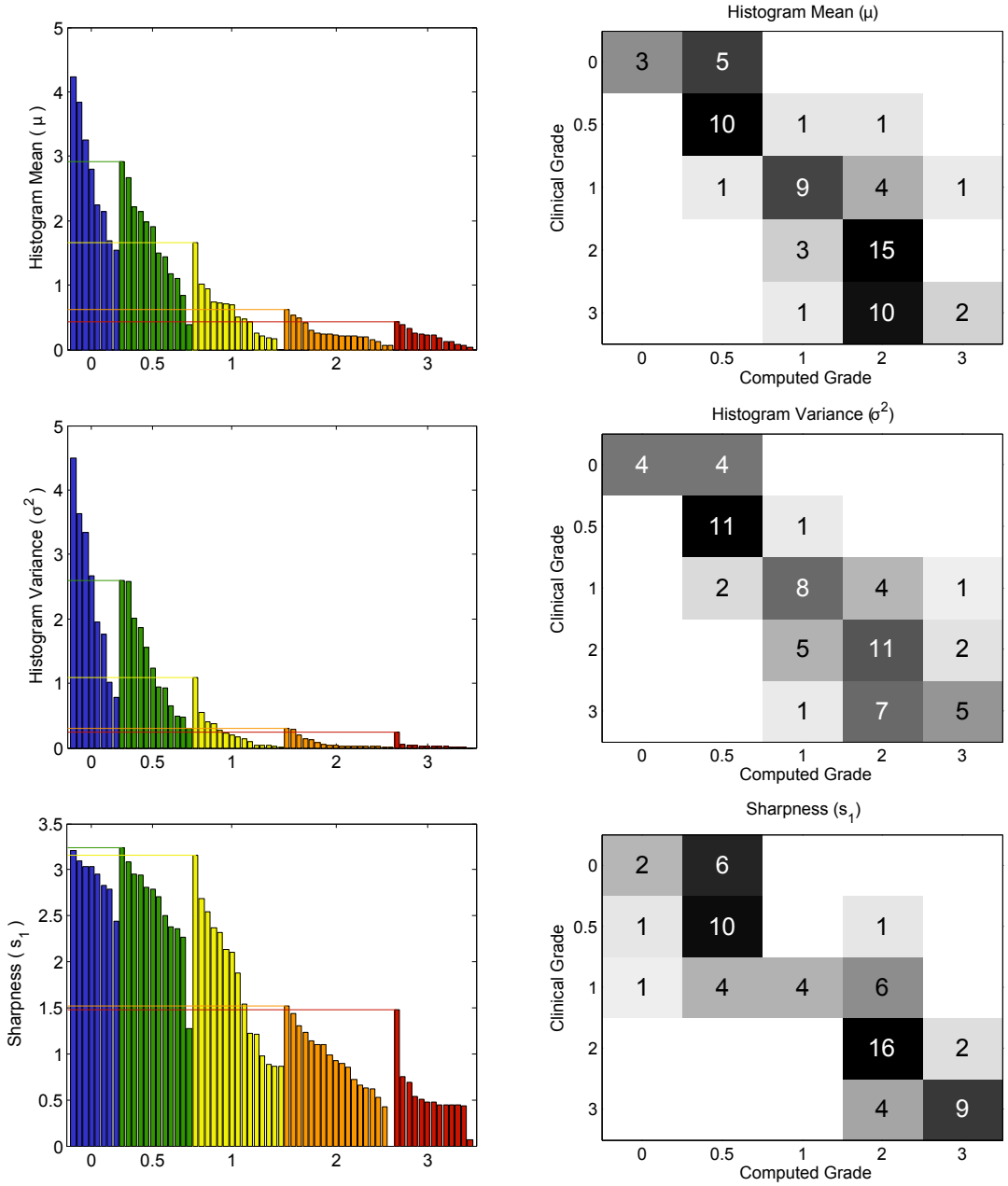

Figure 5.1: Normalized and Sorted Feature Values for Grades & Simple Threshold Classification Results for Each Feature

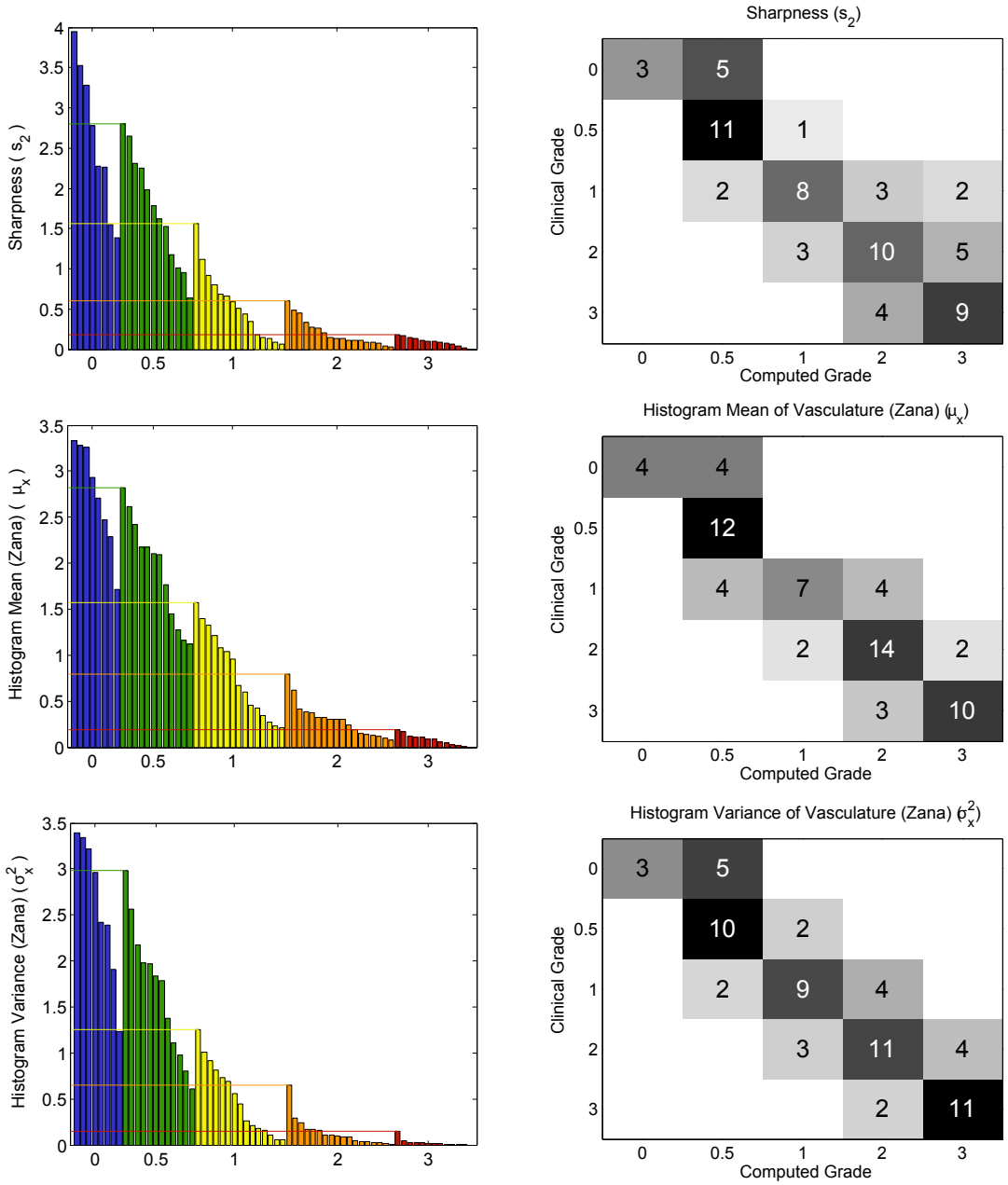

Figure 5.1: Normalized and Sorted Feature Values for Grades & Simple Threshold Classification Results for Each Feature

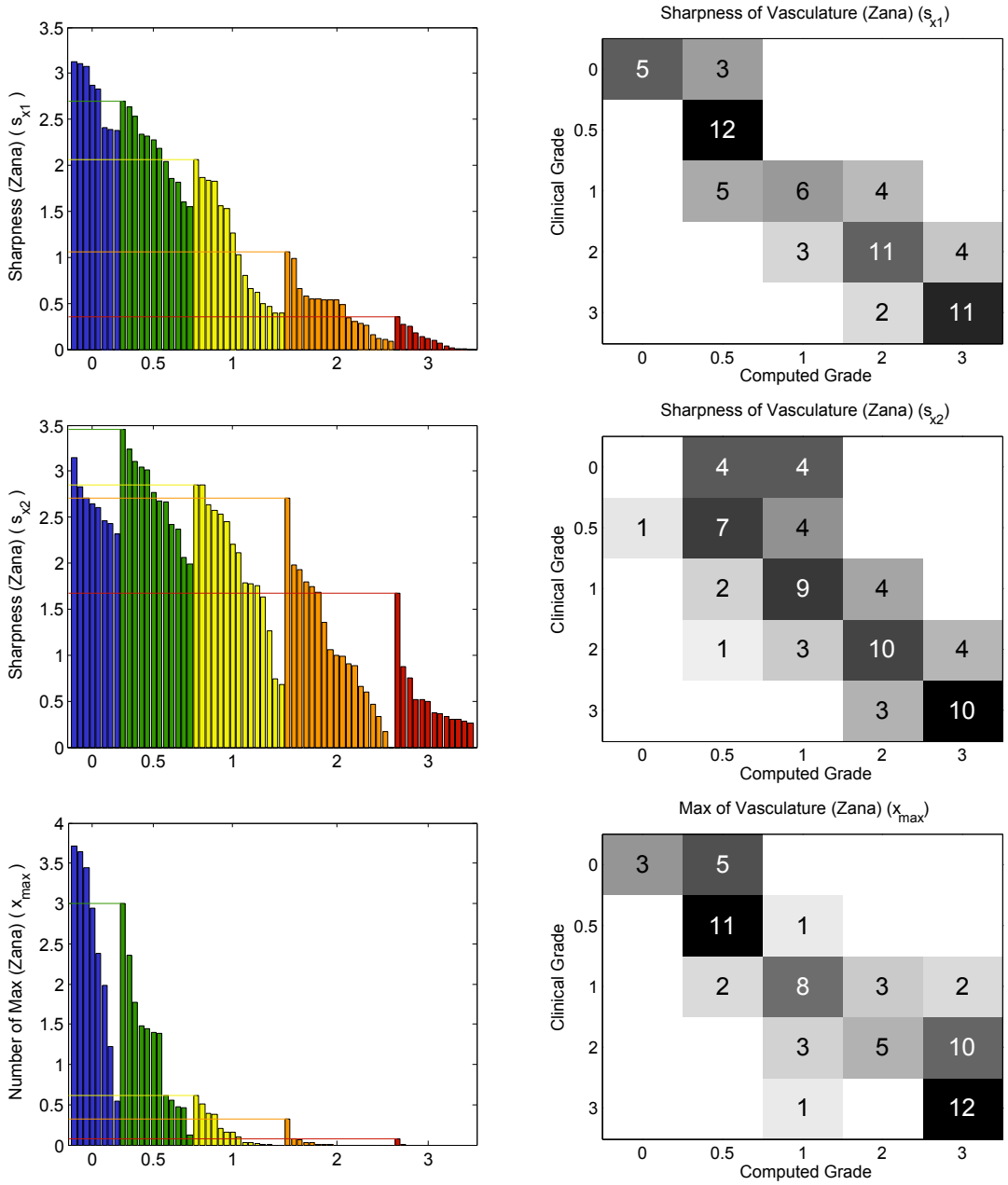

Figure 5.1: Normalized and Sorted Feature Values for Grades & Simple Threshold Classification Results for Each Feature

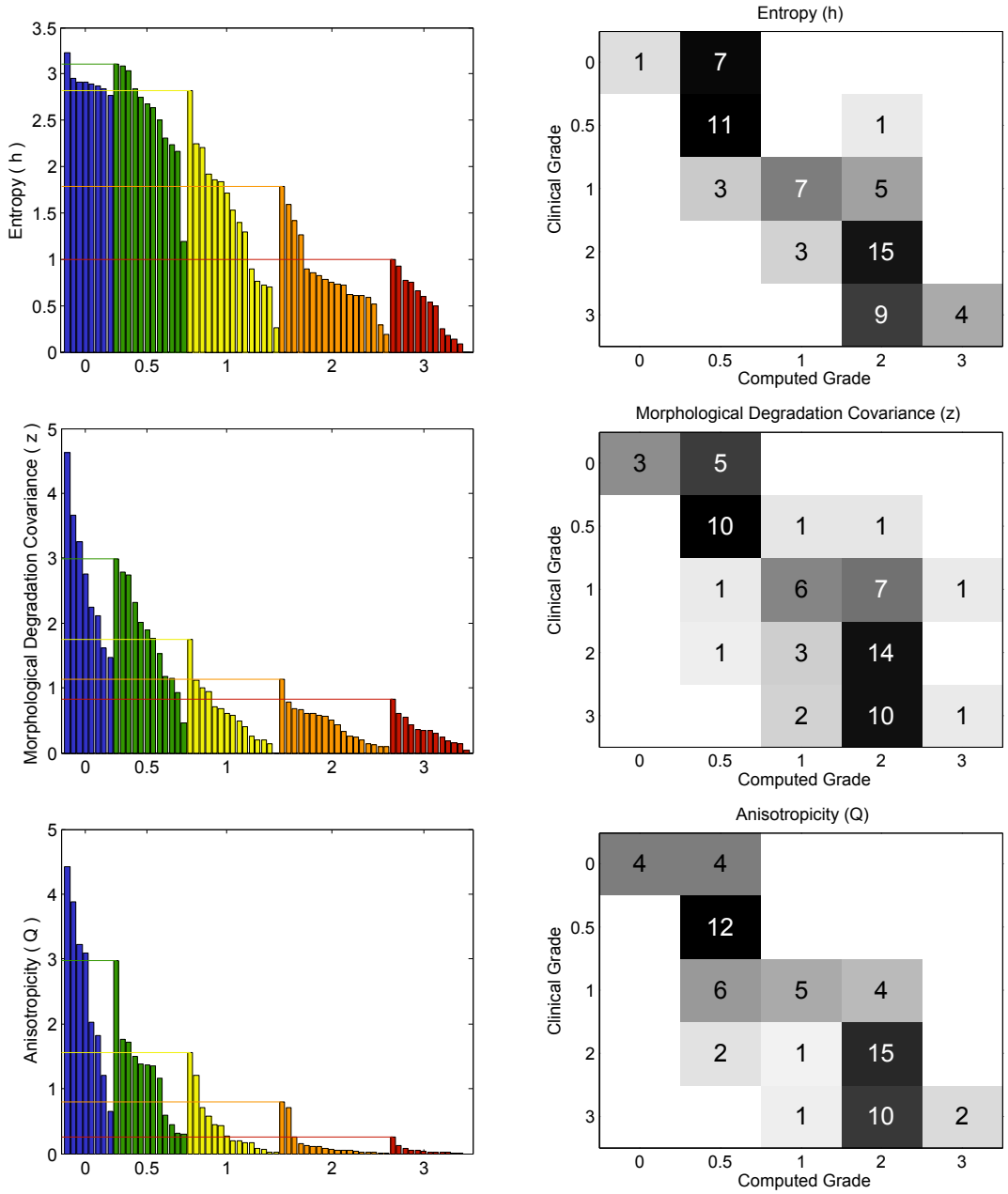

Figure 5.1: Normalized and Sorted Feature Values for Grades & Simple Threshold Classification Results for Each Feature

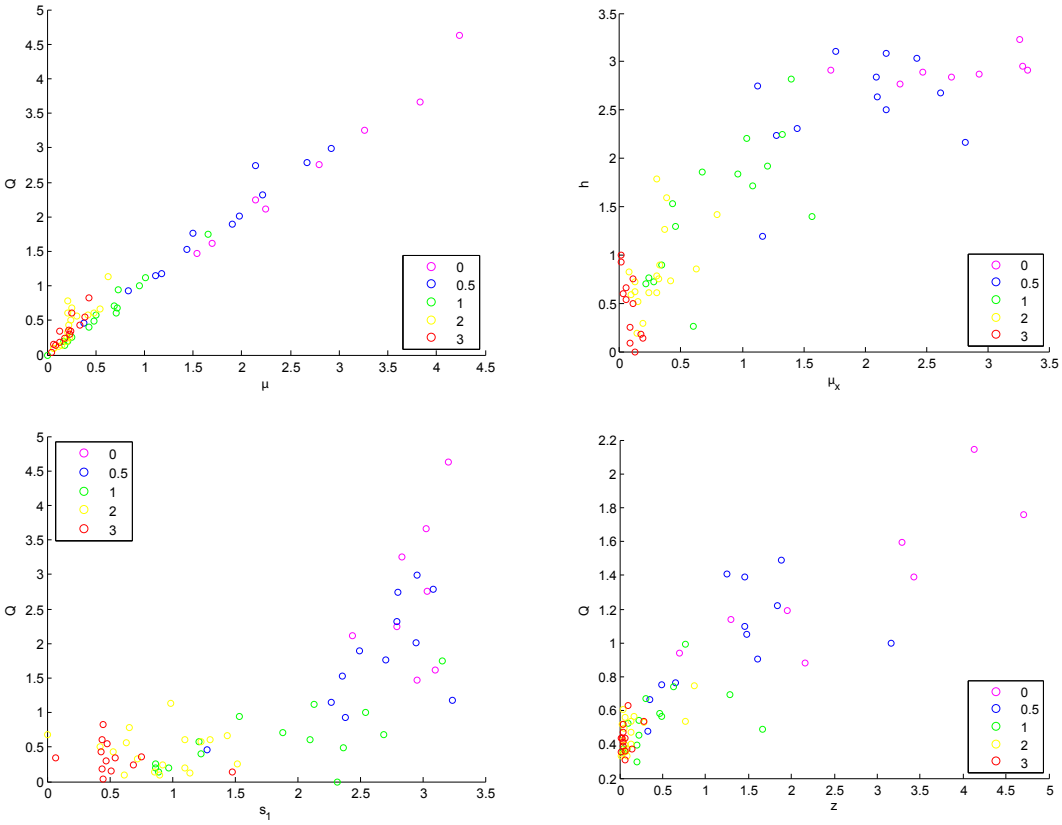

Figure 5.2: 2 Feature Scatter Graphs Showing Correlations

5.2 Classification Results

Leave-one-out validation results for classifiers using different combinations of features are provided in Figure 5.3.

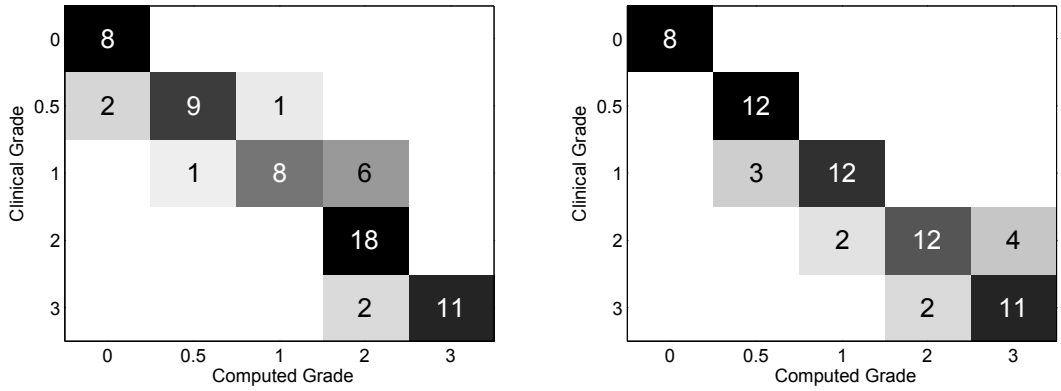

(a) MD, Acc:0.82 (b) SVM, Acc:0.83

Figure 5.3: Classification Results

Manually designed method is one of the most accurate methods. SVM classifier has the greatest accuracy. This is expected, since SVM classifiers are known for their success when the training sets are small.

5.3 Comments on Results

Cases in which automatic grading fails and possible explanations for particular failures are presented in this section.

Reasons that some images are graded as more heavily hazed than they really are (their feature values are lower than the feature values of the images in the same grade class):

- Nonuniform illumination causing outer parts of the image to become underexposed
- Bad focus resembling vitreous haze

- Dark (underexposed) images
- Images with too thin and scarce retinal vasculature due to some diseases

Reasons that some images are graded as less hazy than they really are (their feature values are higher than the feature values of the images in the same grade class):

- Eyes with vitreous haze confined to different regions in patches or images that have haze-free regions
- Bright (overexposed) and clear (high contrast) images
- Diseased retinas with edemas and exudates

In summary, low quality images (nonuniformly illuminated, very dark, very bright or badly focused), thin and scarce retinal vasculatures, diseased retinas (with edemas and exudates), and eyes with vitreous haze confined to different regions in patches create difficulties for current algorithm.

Chapter 6

CONCLUSION

6.1 Summary

In this work, promising results are obtained in automated grading of vitreous haze problem. Several algorithms which are developed for other purposes, are utilized and few novel techniques are introduced. A literature review is provided for methods that are not implemented but may be valuable for further improvements.

6.2 Future Research Directions

Current work depends on a small data set to evaluate success of proposed method. A larger data set should be used in future work. Moreover, when acquiring the data set, using different Bangerter occlusion filters on clear eyes may provide a reliably scored data set. Grade system will be changed to the one in Davis et al. [16].

Problems encountered, when processing the images with low quality and the images of the diseased eyes, should be solved for usability of the method in clinical settings. Further utilization of listed AQA and segmentation algorithms may improve the results.

REFERENCES

[1] Henry Gray. *Anatomy of the human body*. Lea & Febiger, 1918.

[2] Ronan O'Rahilly and Fabiola Müller. *Basic human anatomy: a regional study of human structure*. Saunders Philadelphia, PA, 1983.

[3] B Cassin and SAB Solomon. Dictionary of eye terminology, 1990.

[4] Dale Purves, George J Augustine, David Fitzpatrick, Lawrence C Katz, Anthony-Samuel LaMantia, James O McNamara, and S Mark Williams. *Neuroscience*. Sinauer Associates Inc. Sunderland, MA, 2001.

[5] Stuart Ira Fox. *Human physiology*. McGraw-Hill Higher Education, 2008.

[6] Rui Bernardes, Pedro Serranho, and Conceição Lobo. Digital ocular fundus imaging: a review. *Ophthalmologica*, 226(4):161–181, 2011.

[7] Rajendra Acharya, Wong Li Yun, EYK Ng, Wenwei Yu, and Jasjit S Suri. Imaging systems of human eye: a review. *Journal of medical systems*, 32(4):301–315, 2008.

[8] Ied Alabboud, Gonzalo Muyo, Alistair Gorman, David Mordant, Andrew McNaught, Clement Petres, Yvan R Petillot, and Andrew R Harvey. New spectral imaging techniques for blood oximetry in the retina. In *European Conference on Biomedical Optics*, pages 66310L–66310L. International Society for Optics and Photonics, 2007.

[9] Galina Dimitrova and Satoshi Kato. Color doppler imaging of retinal diseases. *Survey of ophthalmology*, 55(3):193–214, 2010.

[10] Shuliang Jiao, Minshan Jiang, Jianming Hu, Amani Fawzi, Qifa Zhou, K Kirk Shung, Carmen A Puliafito, and Hao F Zhang. Photoacoustic ophthalmoscopy for in vivo retinal imaging. *Optics express*, 18(4):3967–3972, 2010.

[11] Yingxia Li, Haiying Cheng, and Timothy Q Duong. Blood-flow magnetic resonance imaging of the retina. *Neuroimage*, 39(4):1744–1751, 2008.

[12] A Deckert, S Schmitz-Valckenberg, J Jorzik, A Bindewald, FG Holz, and U Mansmann. Automated analysis of digital fundus autofluorescence images of geographic atrophy in advanced age-related macular degeneration using confocal scanning laser ophthalmoscopy (cslo). *BMC ophthalmology*, 5(1):8, 2005.

[13] MF Armaly. Optic cup in normal and glaucomatous eyes. *Investigative Ophthalmology & Visual Science*, 9(6):425–429, 1970.

[14] James L Kinyoun, Donald C Martin, Wilfred Y Fujimoto, and Donna L Leonetti. Ophthalmoscopy versus fundus photographs for detecting and grading diabetic retinopathy. *Investigative ophthalmology & visual science*, 33(6):1888–1893, 1992.

[15] Robert B Nussenblatt, Alan G Palestine, Chi-Chao Chan, and François Roberge. Standardizatlon of vitreal inflammatory activity in intermediate and posterior uveitis. *Ophthalmology*, 92(4):467–471, 1985.

[16] Janet L Davis, Brian Madow, Jessica Cornett, Rick Stratton, Ditte Hess, Vittorio Porciatti, and William J Feuer. Scale for photographic grading of vitreous haze in uveitis. *American journal of ophthalmology*, 150(5):637–641, 2010.

[17] SJ Kimura, Ph Thygeson, and MJ Hogan. Signs and symptoms of uveitis. ii. classification of the posterior manifestations of uveitis. *American journal of ophthalmology*, 47(5, Part 2):171, 1959.

[18] Pietro Perona and Jitendra Malik. Scale-space and edge detection using anisotropic diffusion. *Pattern Analysis and Machine Intelligence, IEEE Transactions on*, 12(7):629–639, 1990.

[19] AA Chernomorets, AS Krylov, AV Nasonov, AS Semashko, VV Sergeev, VS Akopyan, AS Rodin, and NS Semenova. Automated processing of retinal images. In *21-th International Conference on Computer Graphics GraphiCon*, pages 78–81, 2011.

[20] Karel Zuiderveld. Contrast limited adaptive histogram equalization. In *Graphics gems IV*, pages 474–485. Academic Press Professional, Inc., 1994.

[21] Chanjira Sinthanayothin, James F Boyce, Helen L Cook, and Thomas H Williamson. Automated localisation of the optic disc, fovea, and retinal blood vessels from digital colour fundus images. *British Journal of Ophthalmology*, 83(8):902–910, 1999.

[22] Langis Gagnon, Marc Lalonde, Mario Beaulieu, and Marie-Carole Boucher. Procedure to detect anatomical structures in optical fundus images. In *Medical Imaging 2001*, pages 1218–1225. International Society for Optics and Photonics, 2001.

[23] Huiqi Li and Opas Chutatape. Automated feature extraction in color retinal images by a model based approach. *Biomedical Engineering, IEEE Transactions on*, 51(2):246–254, 2004.

[24] Meindert Niemeijer, Michael D Abràmoff, and Bram Van Ginneken. Segmentation of the optic disc, macula and vascular arch in fundus photographs. *Medical Imaging, IEEE Transactions on*, 26(1):116–127, 2007.

[25] Meindert Niemeijer, Michael D Abràmoff, and Bram Van Ginneken. Fast detection of the optic disc and fovea in color fundus photographs. *Medical image analysis*, 13(6):859–870, 2009.

[26] Subhasis Chaudhuri, Shankar Chatterjee, Norman Katz, Mark Nelson, and Michael Goldbaum. Detection of blood vessels in retinal images using two-dimensional matched filters. *IEEE Transactions on medical imaging*, 8(3):263–269, 1989.

[27] Frederic Zana and J-C Klein. Segmentation of vessel-like patterns using mathematical morphology and curvature evaluation. *Image Processing, IEEE Transactions on*, 10(7):1010–1019, 2001.

[28] Henk Heijmans, Michael Buckley, and Hugues Talbot. Path openings and closings. *Journal of Mathematical Imaging and Vision*, 22(2-3):107–119, 2005.

[29] Joao VB Soares, Jorge JG Leandro, Roberto M Cesar, Herbert F Jelinek, and Michael J Cree. Retinal vessel segmentation using the 2-d gabor wavelet and supervised classification. *Medical Imaging, IEEE Transactions on*, 25(9):1214–1222, 2006.

[30] Samuel C Lee and Yiming Wang. Automatic retinal image quality assessment and enhancement. In *Medical Imaging'99*, pages 1581–1590. International Society for Optics and Photonics, 1999.

[31] Marc Lalonde, Langis Gagnon, and MC Boucher. Automatic image quality assessment in optical fundus images. Technical report, CRIM Report CRIM-00/12-11, ISBN-2-89522-006-9, 2000.

[32] DB Usher, M Himaga, MJ Dumskyj, and JF Boyce. Automated assessment of digital fundus image quality using detected vessel area. In *Proceedings of Medical Image Understanding and Analysis*, pages 81–84, 2003.

[33] Alan D Fleming, Sam Philip, Keith A Goatman, John A Olson, and Peter F Sharp. Automated assessment of diabetic retinal image quality based on clarity and field definition. *Investigative ophthalmology & visual science*, 47(3):1120–1125, 2006.

[34] Alexandra A Chernomorets and Andrey S Krylov. Blur detection in fundus images. In *Biomedical Engineering and Informatics (BMEI), 2012 5th International Conference on*, pages 243–246. IEEE, 2012.

[35] Luca Giancardo, MD Abramoff, E Chaum, TP Karnowski, F Meriaudeau, and KW Tobin. Elliptical local vessel density: a fast and robust quality metric for retinal images. In *Engineering in Medicine and Biology Society, 2008. EMBS 2008. 30th Annual International Conference of the IEEE*, pages 3534–3537. IEEE, 2008.

[36] Thomas Kohler, Attila Budai, Martin F Kraus, Jan Odstrcilik, Georg Michelson, and Joachim Hornegger. Automatic no-reference quality assessment for retinal fundus images using vessel segmentation. In *Computer-Based Medical Systems (CBMS), 2013 IEEE 26th International Symposium on*, pages 95–100. IEEE, 2013.

[37] Jan Paulus, Jörg Meier, Rüdiger Bock, Joachim Hornegger, and Georg Michelson. Automated quality assessment of retinal fundus photos. *International journal of computer assisted radiology and surgery*, 5(6):557–564, 2010.

[38] Robert M Haralick, Karthikeyan Shanmugam, and Its' Hak Dinstein. Textural features for

image classification. *Systems, Man and Cybernetics, IEEE Transactions on*, (6):610–621, 1973.

[39] Meindert Niemeijer, Michael D Abramoff, and Bram van Ginneken. Image structure clustering for image quality verification of color retina images in diabetic retinopathy screening. *Medical image analysis*, 10(6):888–898, 2006.

CURRICULUM VITAE

SERHAT VAROLGÜNEŞ was born in Diyarbakır on December 15, 1991. He graduated from Ortadoğu College in 2007. He received his B.S. degree in Electrical and Electronics Engineering from Middle East Technical University (METU), Ankara, Turkey, in 2011. He received his M.S. degree under the supervision of Prof. Alper Demir in Biomedical Sciences and Engineering from Koc University, Istanbul, Turkey in 2015. At the same time, he was both research and teaching assistant in the Computational and Quantitative Biology Laboratory, Koc University. His current research interests include neuroscience and image proccessing.